NUMERICAL SIMULATION AND EXPERIMENTAL VALIDATION OF TEXTURE IN EXTRUDED WIRES OF A BCC METAL

MENGYIN XIE[*], NIKOLAOS BAIMPAS[*], CHRISTINA REINHARD[†] AND ALEXANDER M. KORSUNSKY[*]

[*] Department of Engineering Science
University of Oxford, Parks Road, Oxford OX1 3PJ, UK
e-mail: alexander.korsunsky@eng.ox.ac.uk, www.eng.ox.ac.uk/elasticity

[†] Diamond Light Source Ltd.
Didcot, Oxfordshire OX11 0DE

Key words: Computational Plasticity, Texture, Extrusion, Synchrotron X-ray Diffraction.

Abstract. We present a comparison between a viscoplastic crystal plasticity finite element simulation of the extrusion process applied to a bcc polycrystal and the experimental evaluation of the preferred orientation (texture) in a tungsten wire by monochromatic synchrotron X-ray diffraction with an area detector. We perform a numerical simulation of sample texture evolution during large extrusion deformation with the elongation factor up to the value of fifty. By matching the predicted Orientation Distribution Functions (ODF) and the pole figures generated on the basis of the simulations to the experimental observations, the extrusion strain experienced by the sample during processing can be estimated.

1 INTRODUCTION

Deformation processing of metallic alloy systems continues to account for a significant fraction of all fabrication operations carried out in structural engineering. In addition, a number of novel processing routes have been developed in recent decades and years that open up new possibilities, such as solid-state joining of (dissimilar) metallic samples by linear friction welding or inertia friction welding; severe plastic deformation processing by equal channel angular extrusion or high pressure torsion to induce grain refinement (nano-structuring) and amorphisation, etc. All these processes make direct use of the high deformability of metallic samples the leads to large overall strains being attained, and that are accompanied by large grain deformation and rotation. An important consequence of large strain processing is the alignment of the intragranular crystal lattices with certain global directions. This process is driven by the anisotropy of material's mechanical properties at the level of individual grains, both in terms of elastic constants, and plastic strength. As a consequence, the overall mechanical properties of the polycrystal may also acquire a high degree of anisotropy, and may become reflected in the sample or component response to loading, fatigue durability, etc.

The current study was aimed at combining numerical modeling of grain deformation and re-orientation (both in terms of grain shape, i.e. morphology, and lattice rotation) with

experimental evaluation of texture using diffraction of penetrating radiation (synchrotron X-rays). We chose an extruded tungsten wire as an example for this investigation.

2 EXPERIMENTAL SETUP AND TEXTURE INTERPRETATION

The extruded Tungsten wire is with diameter of 0.1 mm. The diffraction pattern was taken at beamline I12 (JEEP), Diamond Light Source, Didcot, Oxfordshire, UK. The diffraction setup was typical Debye-Scheerer setup mainly consists of an area detector (Thales Pixium RF4343). The detector has an active area of 2880 × 2881 pixels, and the size of each pixel is 148 × 148 μm^2. Through two groups of slits, the beam size was adjusted to 100 × 100 μm^2, which just covers the diameter of the sample. The beam energy was set to 100 KeV, and the sample to detector distance was 1178.41 mm.

An example Debye-Scherrer diffraction pattern is shown in Fig 1.a. Due to the fact that the beam energy is relatively high, many Bragg diffraction rings are captured by the detector. The more Bragg peaks are probed, the more accurate is the calculated texture interpretation. Here, we only analyze the following four reflection rings: (110), (200), (211) and (310). They are the lowest order reflection peaks for BCC materials. Althought the (220) peak is of lower order than (310), it contains the same texture information as (110), so it has been ignored.

We present two distinct methods to estimate orientation distribution function (full texture information) from a single multi-peak Debye-Scherrer pattern, and the details of the procedures can be found in [1]. The first method is based on the pole figure evaluation directly from the experimental data, and ODF estimation on this basis by MTEX [2]. The pattern was binned azimuthally into 72 portions with 5º azimuthal width. Then single peak (Gaussian) fitting was performed for the 72 line profiles to compute the integrated intensity for the (110), (100), (211) and (310) peaks. Finally, these integrated intensities were projected onto a circular area according to the equal area geometric projection used to form raw pole figures (as shown in Fig 1.b). The four raw pole figures were then imported into MTEX. In MTEX, any ODF is considered as the linear combination of radially symmetric "bell-shaped" functions in 3D Euler space. It employs a modified least square fitting algorithm to determine the coefficients of those "bell-shape" functions by matching raw pole figures with the projections of the ODF. Fig 2.a shows the projections (full pole figures) of the estimated ODF from the raw pole figures. The intensity that appears in the full pole figures refers to the probability to find a (*hkl*) plane normal at that pole and is called "multiples of a random distribution" (MRD). MRD is a normalized property of the integrated intensity in the raw pole figure, and the normalization is automatically done by MTEX. The pole figure maxima (PFM) in Fig 2.a match the ones in Fig 1.b well. A detailed analysis [1] has shown that although the raw pole figures appear only to cover a small area of the circle, it is nevertheless possible to determine the overall ODF for the diffraction volume with satisfactory accuracy.

The second ODF determination approach consists of Rietveld full pattern analysis and the application of the extended-WIMV algorithm. The main idea of this approach is to fit the 2D diffraction pattern directly and by using the extended-WIMV algorithm to determine the volume of fraction of the discrete ODF components. Since this is a discrete approach, the calculated ODF turns to be not as smooth as that determined by the MTEX method. This is seen by the comparison between Fig 2. a and b. The 2D patterns in Fig 2. a and b match well, although the intensity looks slightly different. It is easy to associate those pole figures with a

typical extrusion texture. The (110) plane normal is found to be parallel to the extrusion direction. The others plane normals (200), (211) and (310) are axi-symmetrically distributed around the extrusion direction.
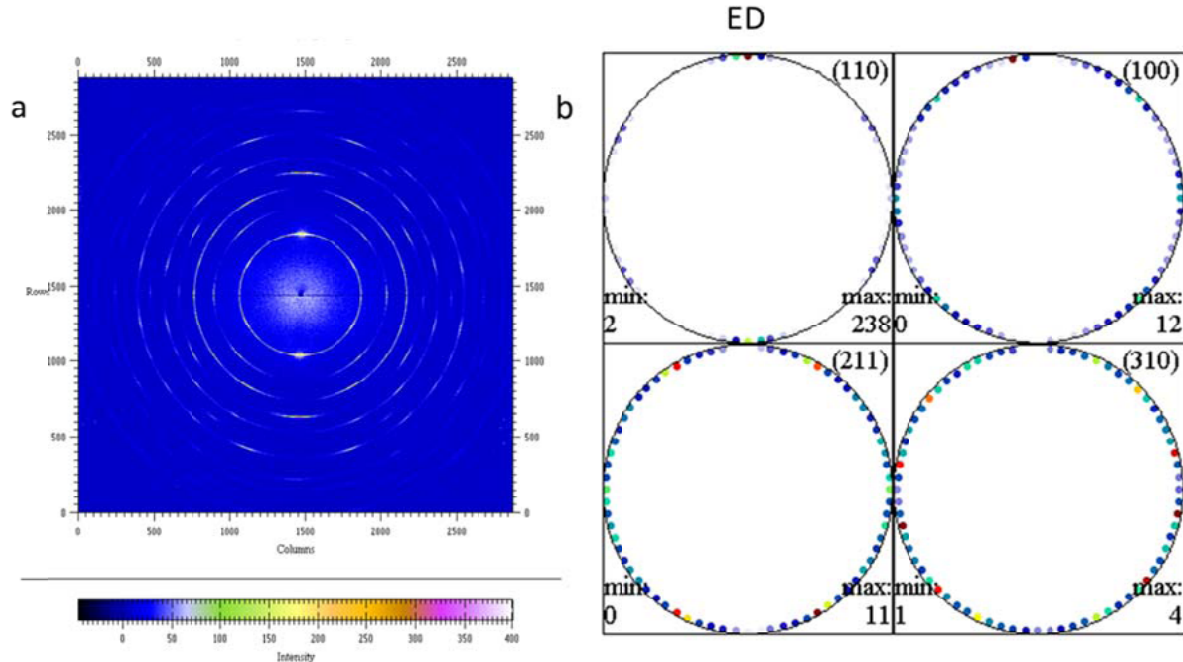

Fig 1. A single Debye-Scherrer diffraction pattern (a) of Tungsten wire; (b) four raw pole figures from this Debye-Scherrer pattern after single peak fitting and equal area projection. ED stands for extrusion direction.
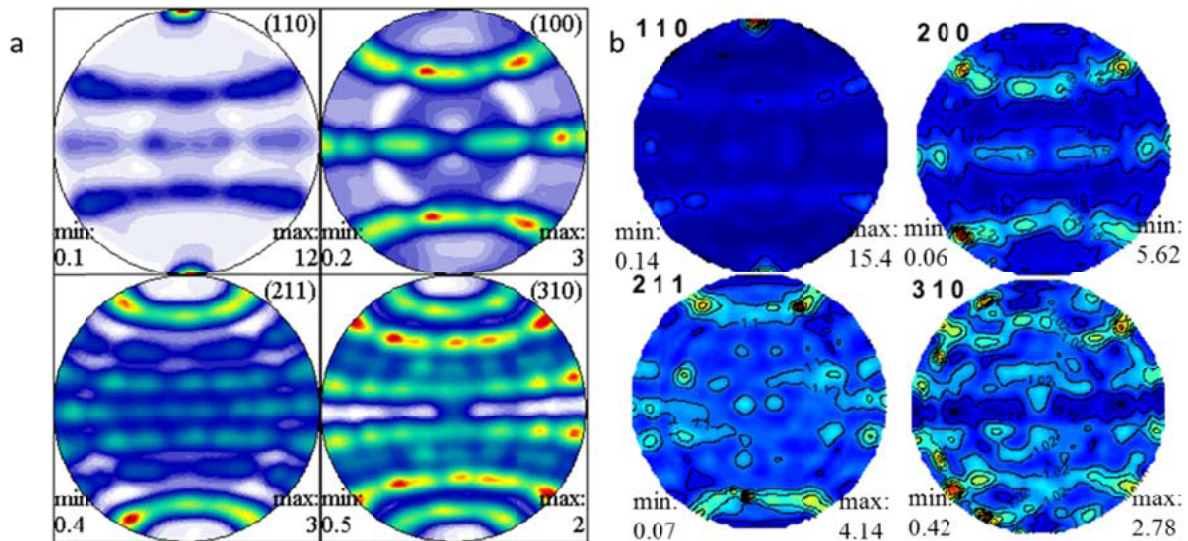

Fig 2. Full pole figure calculated by (a) MTEX and (b) by Rietveld refinement.

3 CRYSTAL PLASTICITY FINITE ELEMENT MODELLING

3.1 Framework for crystal plasticity simulation

The extrusion process of the Tungsten wire was modeled using crystal plasticity finite element (CPFE) framework [3]. In crystal plasticity the plastic deformation is considered to

be the result of dislocation slip on certain crystal planes. Since texture change of polycrystalline materials is often associated with large plastic deformation, large strain theory is used. The key constitutive equations used in the formulation are listed below.

Kinematics:

The total deformation gradient $\mathbf{F}$ can be decomposed into the elastic and plastic parts,

$$\mathbf{F} = \mathbf{F}^e + \mathbf{F}^P \tag{1}$$

where the superscripts e and p stand for elastic and plastic deformation, respectively.

The total velocity gradient is given by

$$\mathbf{L} = \dot{\mathbf{F}}(\mathbf{F}^{-1}) = \dot{\mathbf{F}}^e(\mathbf{F}^e)^{-1} + \dot{\mathbf{F}}^e\dot{\mathbf{F}}^P(\mathbf{F}^P)^{-1}(\mathbf{F}^e)^{-1} = \mathbf{L}^e + \mathbf{L}^P \tag{2}$$

The shear (slip) deformation that happens on slip systems indexed by α causes the plastic deformation gradient given by

$$\mathbf{F}^P = \mathbf{I} + \gamma^\alpha(\mathbf{s}^\alpha \times \mathbf{n}^\alpha) \tag{3}$$

where unit vectors $\mathbf{s}^\alpha$ and $\mathbf{n}^\alpha$ are the slip direction and normal to slip plane in the lab coordinates, respectively, and γ^α is the Taylor cumulative shear strain on the α slip systems.

The $\dot{\mathbf{F}}^P \cdot (\mathbf{F}^P)^{-1}$ is then the sum of the slipping rate $\dot{\gamma}^{(\alpha)}$ over all the slip systems,

$$\dot{\mathbf{F}}^P \cdot (\mathbf{F}^P)^{-1} = \sum_\alpha \dot{\gamma}^\alpha(\mathbf{s}^\alpha \times \mathbf{n}^\alpha) \tag{4}$$

Plastic deformation does not change the slip direction and the normal direction to slip plane vectors, hence only the elastic part of the deformation gradient is considered to determine this phenomenon,

$$\mathbf{s}^{*\alpha} = \mathbf{F}^e \cdot \mathbf{s}^\alpha \tag{5}$$
$$\mathbf{n}^{*\alpha} = \mathbf{n}^\alpha \cdot (\mathbf{F}^e)^{-1}$$

where the star (*) stands for the parameter modified by elastic deformation.

The velocity gradient $\mathbf{L}$ can be decomposed into a pure stretch ($\mathbf{D}$) and pure skew part ($\mathbf{\Omega}$),

$$\mathbf{L} = \mathbf{D} + \mathbf{\Omega} \tag{6}$$

Both $\mathbf{D}$ and $\mathbf{\Omega}$ can also be decomposed into the elastic and plastic parts,

$$\mathbf{D} = \mathbf{D}^e + \mathbf{D}^P \tag{7}$$
$$\mathbf{\Omega} = \mathbf{\Omega}^e + \mathbf{\Omega}^P$$

The elastic part and plastic parts of the velocity are,

$$\mathbf{L}^e = \mathbf{D}^e + \mathbf{\Omega}^e = \dot{\mathbf{F}}^e(\mathbf{F}^e)^{-1} \tag{8}$$
$$\mathbf{L}^P = \dot{\mathbf{F}}^e\dot{\mathbf{F}}^P(\mathbf{F}^P)^{-1}(\mathbf{F}^e)^{-1} = \mathbf{D}^P + \mathbf{\Omega}^P = \sum_\alpha \dot{\gamma}^\alpha(\mathbf{s}^{*\alpha} \times \mathbf{n}^{*\alpha})$$

The $\mathbf{\Omega}^P$ and $\mathbf{D}^P$ are given by

$$\mathbf{D}^P = \frac{1}{2}(\mathbf{s}^{*\alpha} \times \mathbf{n}^{*\alpha} + \mathbf{n}^{*\alpha} \times \mathbf{s}^{*\alpha})\,\dot{\gamma}^\alpha \tag{9}$$

$$\mathbf{\Omega}^P = \frac{1}{2}(\mathbf{s}^{*\alpha} \times \mathbf{n}^{*\alpha} - \mathbf{n}^{*\alpha} \times \mathbf{s}^{*\alpha})\,\dot{\gamma}^\alpha$$

Power law and hardening:

The shear deformation here is approximated by power law [4]

$$\dot{\gamma}^\alpha = \dot{\gamma}_0 sign(\tau^\alpha)\left(\frac{|\tau^\alpha|}{g^\alpha}\right)^{1/m} \tag{10}$$

where $\dot{\gamma}^\alpha$ is the shear rate on the α slip system, $\dot{\gamma}_0$ is the initial shear rate on the α slip system, τ^α is the resolved shear stress on the α slip system, and g^α is the slip resistance.

The strain hardening is characterized by the evolution of the slip resistance g^α with time,

$$\dot{g}^\alpha = \sum_\beta h_{\alpha\beta} \dot{\gamma}^\beta \tag{11}$$

In [5], the self-hardening moduli were suggested to be represented by

$$h_{\alpha\alpha} = h(\gamma) = h_0 sech^2 \left| \frac{h_0 \gamma}{\tau_s - \tau_0} \right| \tag{12}$$

$$h_{\alpha\beta} = qh(\gamma)$$

where h_0 is the initial hardening modulus, τ_0 is the yield slip resistance and equals to the initial value of current strength $g^\alpha(0)$, τ_s is the initial (stage I) cristical resolved shear stress that is one of the starting input parameters of the model, q is a constant, and γ is the Taylor cumulative shear strain on all slip systems, i.e.

$$\gamma = \sum_\alpha \int_0^t |\dot{\gamma}^\alpha| dt \tag{13}$$

Texture update:
Since only the elastic spin matrix causes change in the grain orientation, finite rotation theory is used to update the grains orientation at each increment. The rotation increment matrix is given by:

$$\Delta \mathbf{R} = (\mathbf{\Omega}^e \cdot dt) \cdot \mathbf{R}_{t0} \tag{14}$$

The resulting rotation at time $t0 + \Delta t$ is given by

$$\mathbf{R}_{t0+\Delta t} = \mathbf{R}_{t0} + \Delta \mathbf{R} \tag{15}$$

3.2 Boundary conditions and the Representative Volume Element (RVE)

Fig. 3 shows a typical extrusion manufacturing process. A thick wire with a diameter d_1 is pushed through a hard die. The diameter of the wire is reduced to d_0 after extrusion. This process is equivalent to either a uniaxial tension with Z axis being the tensile axis, or a biaxial compression in the X-Y plane.

The strain rate tensors for the two cases have a similar diagonal form. A cubic RVE was created in ABAQUS CAE consisting of $12 \times 12 \times 12 = 1728$ C3D8R elements (8-noded linear cubic). Since each element had only one integration point, enhanced hourglass control was used to ensure numerical stability. Although it is possible to choose elements with more integration points, this would not give significant improvement in the accuracy of simulation, but would increase the computational expense massively. The above crystal plasticity constitutive equations were implemented as a user subroutine (UMAT) [6] within ABAQUS Standard simulation software. Each integration point was assigned a grain orientation using three Euler angles in the Bunge conventions. Therefore, the RVE represented apolycrystalline aggregates with 1728 individual grains.

Tungsten crystals have a body-centered-cubic (BCC) structure for which we only consider the {110} <111> slip system as the vehicle for plastic deformation. Elastic constants for tungsten were taken to be $C_{11} = 522390$ MPa, $C_{12} = 204730$ MPa, $C_{44} = 160830$ MPa [7]. In eqaition (10), the initial shear rate $(\dot{\gamma}_0)$ was set to 0.001 s^{-1}, and m was given the value of 10. In equation (12), the initial hardening modulus (h_0) was set to 1000 MPa, and saturation stress (τ_s) and initial critical resolved shear stress were set to 400 MPa and 200 MPa respectively. The constant q was chosen to be equal to 1.4. Fig. 4 shows the shape change of

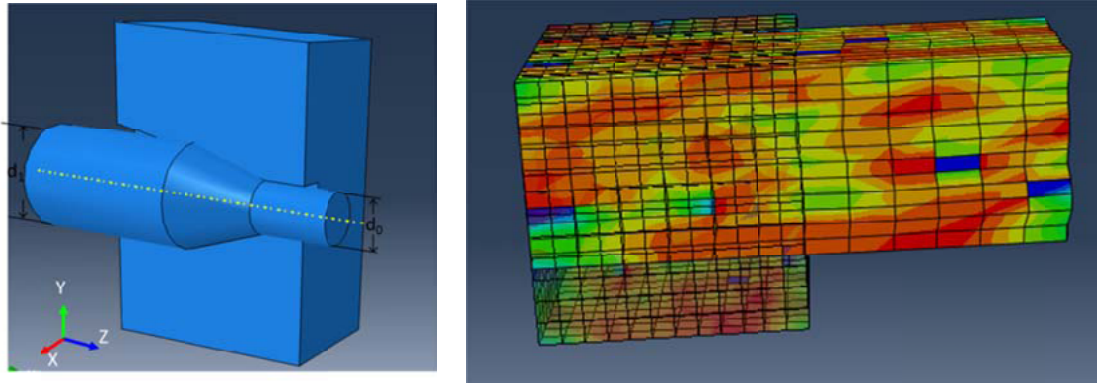the RVE before under uniaxial deformation to $\varepsilon_{33} = 1.0$.

Fig.3. Illustration of extrusion.   Fig.4. RVE shape change after uniaxial deformation to strain value of unity.
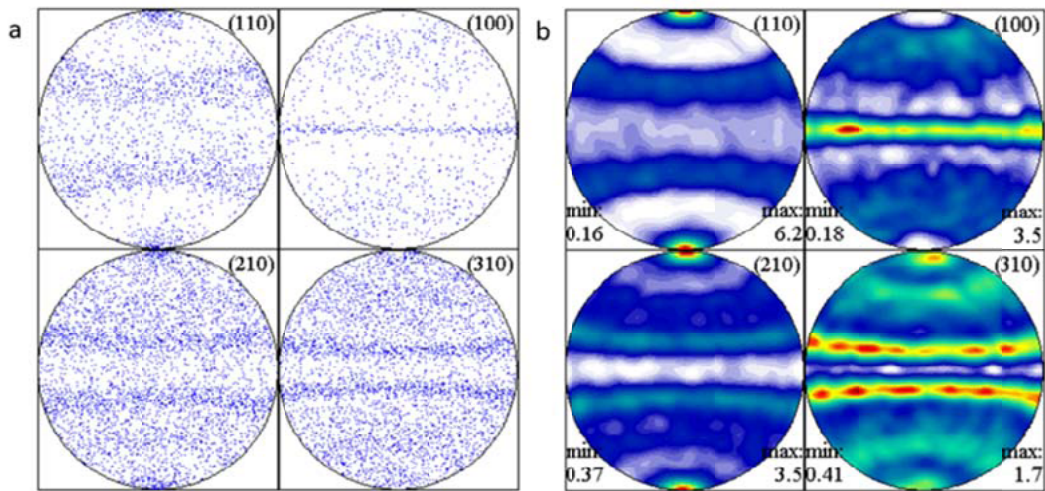

Fig 5. (a) Scatter plots and (b) contour plots of pole figures at $\varepsilon_{33} = 1.0$

Once ABAQUS calculation finished, the orientations of all the integration points after the final increment were extracted from the results file and imported into MTEX. The scatter plot form of the pole figures for the deformation illustrated in Fig. 4 are shown in Fig 5.a. In order to perform quantitative comparison with experimental results, the ODF was estimated from these scatter plot data using MTEX. The same angular parameters (5° half-width for the bell-shaped functions, and 5° for the ODF resolution) were used as in the experimental analysis, to ensure consistency. Fig 5(b) shows the projections of the calculated ODF as the contour plot form of pole figures shown in Fig 5(a).

3.3 Comparison between experiment and modelling

In order to perform quantitative assessment of the match between different ODF's, in particular between those obtained from the experiment and modelling, the measure of ODF difference was defined as follows:

$$e = \frac{\sum_{i}(f_1(g_i) - f_2(g_i))^2}{\sum_{i} f_1(g_i)^2},\qquad(15)$$

where f_1 and f_2 are the volume of fractions of each orientation, and g_i is grain orientation.
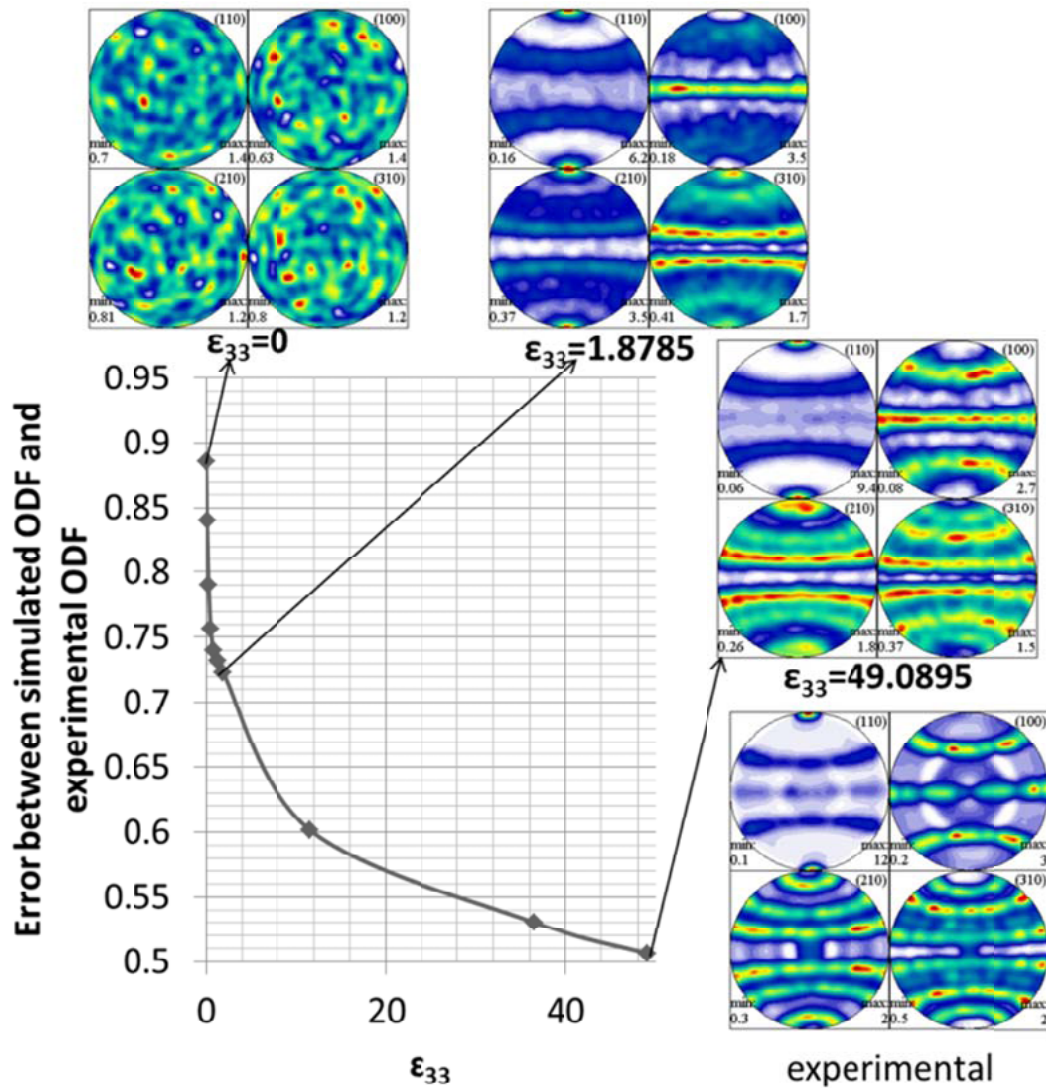
Fig 6. Texture and ODF mismatch evolution with increasing tensile strain.

Fig.6 shows the compassion between the experimental data and the simulation results. At $\varepsilon_{33} = 0$, the RVE is represented by randomly distributed grain orientations, and the pole figures does not show any maxima (PFM's). When the tensile strain along the Z axis was increased to 1.8758, the pole figures began to show similarities with those known to correspond to the typical extrusion texture in BCC metals. The (110) plane normal is found to become parallel with the extrusion direction. However, it is also worth noting that the (210) plane normal became aligned with the extrusion direction, which is not true for the experimental data. The tensile strain was further increased to 49 (the convergence limit for the tension deformation mechanism. The simulated pole figures obtained for at $\varepsilon_{33} = 49$ appear to be more similar to the experimental data compared to those for $\varepsilon_{33} = 1.8785$. Note that the (210) pole figures indicate that the PFM is no longer aligned with the extrusion direction, but becomes axi-symmetrically distributed around the extrusion direction. The curve for the error parameter e indicates the mismatch monotonically decreasing down as the tensile strain

increases. It would be ideal to find a minimal error position at a certain tensile strain that corresponds to the real strain applied to the sample during processing. However, the finite element modeling reaches the convergence limit for the one-step extrusion process simulation. Further improvement would be to consider a two-step extrusion process, *i.e.* deform the RVE to its limit in the first step and then assign the deformed ODF into a new cubic RVE to deform it in the second step. This way much higher values of the tensile strain can be attained. We note that very high values of tensile strain are expected for the real extrusion process, as indicated by the as-received sample diameter of 0.1 mm.

4 CONCLUSIONS

The results reported above represent our attempt to bring together, in a systematic way, the experimental and modelling approaches to texture analysis. On the one hand, we advocate the use of high energy monochromatic synchrotron X-ray diffraction as a means of fast and efficient 'one-shot' texture determination. On the other hand, we present the outline of the formulation and the results of CPFE numerical simulation of large deformations that typically take place during metal processing operations such as forging, extrusion, rolling, welding, etc. We describe how the data obtained from both approaches can be post-processed to derive ODF's, and introduce an important measure for ODF mismatch that allows quantitative assessment of the "goodness" of fit between different measurements and simulations.

REFERENCES

[1] Xie, M.-Y., et al., *Preferred orientation analysis in cubic phase metallic polycrystals by "one-shot" high energy monochromatic synchrotron X-ray diffraction.* Journal of Applied Crystallography (2013) **submitted**.

[2] Hielschera, R. and Schaebena, H., *A novel pole figure inversion method: specification of the MTEX algorithm*, J. Appl. Cryst. (2008) **41**: 1024–1037.

[3] Bower, A.F., *Applied Mechanics of Solids*. Taylor & Francis, (2011).

[4] Roters, F., et al., *Overview of constitutive laws, kinematics, homogenization and multiscale methods in crystal plasticity finite-element modeling: Theory, experiments, applications.* Acta Materialia (2010) **58**(4): 1152-1211.

[5] Peirce, D., R.J. Asaro, and A. Needleman, *An analysis of nonuniform and localized deformation in ductile single crystals.* Acta Metallurgica (1982) **30**(6): 1087-1119.

[6] Huang, Y., *A User-material Subroutine Incorporating Single Crystal Plasticity in the ABAQUS Finite Element Program*. Harvard Univ. Report, (1991).

[7] Kocks, U.F., Tomé, C.N., Wenk, H.-R., Beaudoin, A.J. and Mecking,H., *Texture and Anisotropy – Preferred Orientations in Polycrystals and Their Effect on Materials Properties*. Cambridge University Press, (2000).